Inorganic Chemistry

pubs.acs.org/IC

Article

Synthesis of Zintl Phase Metal Silicide Thermoelectric Materials in Magnesium/Zinc Flux

Amirhossein Zareihassangheshlaghi, Jorge Galeano-Cabral, Md Sahab Uddin, Benny Schundelmier, Kaya Wei, Ryan E. Baumbach, and Susan E. Latturner*

Cite This: https://doi.org/10.1021/acs.inorgchem.4c01079

Read Online

ACCESS | Metrics & More | Article Recommendations | Supporting Information

ABSTRACT: Zintl phases have potential applications as thermoelectric materials for power generation and cooling owing to their complex crystal structures and unique electronic properties. We carried out reactions of silicon with barium and strontium in excess Mg/Zn flux to synthesize $(Ba/Sr)_{5+x}Mg_{19-x}Si_{12}$ Zintl phases, investigating the effect of varying Ba/Sr ratio on site mixing and thermoelectric properties. $(Ba/Sr)_{5+x}Mg_{19-x}Si_{12}$ compounds with $0 < x < 3$ are charge-balanced Zintl phases which adopt the hexagonal $Ho_5Ni_{19}P_{12}$ structure type (space group $P\bar{6}2m$). Density of states calculations indicate that these materials are semimetals. Single-crystal X-ray diffraction data and elemental analysis for $Ba_5Mg_{19}Si_{12}$, $Ba_{4.86}Sr_{2.94}Mg_{16.20}Si_{12}$, $Ba_{3.63}Sr_{4.20}Mg_{16.17}Si_{12}$, $Ba_{1.93}Sr_{5.99}Mg_{16.08}Si_{12}$, and $Sr_{7.82}Mg_{16.18}Si_{12}$ show occupation of barium and strontium cations in Ho sites, while strontium mixes with magnesium on a specific Ni site. Powder XRD data of products show that they are single phase throughout the sample. Thermoelectric measurements indicate that increasing strontium content and mixing on three cation sites decreases thermal conductivity; it is hypothesized that improved overall thermoelectric behavior is likely due to the rattling of the Sr cations in their positions.

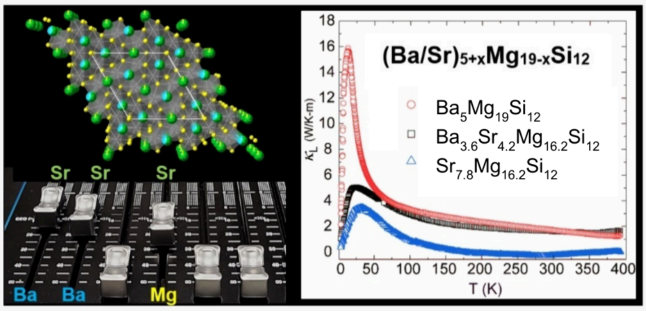

INTRODUCTION

Thermoelectric materials generate an electric potential in response to a temperature difference across them (Seebeck effect) or, alternatively, create a temperature difference when subjected to an electric potential (Peltier effect).[1] These behaviors can be used for waste heat recovery or electronic cooling. Thermoelectric response is dependent on the Seebeck coefficient S, electrical conductivity σ, and thermal conductivity κ (which is the sum of contributions from electron motion and lattice vibration).[1,2] In thermoelectric materials, achieving an optimal figure of merit zT ($zT = [S^2\sigma/(\kappa_e + \kappa_L)]T$) is crucial for enhancing the efficiency of energy conversion from heat to electricity, and vice versa. The lattice thermal conductivity (κ_L) serves as an autonomously adjustable factor, representing the most straightforward method for improving the figure of merit by reducing the thermal conductivity without adversely affecting the electrical properties. An effective way to reduce κ_L is to introduce disorder by substitution and doping.[1,3−6] Aliovalent doping can modify the number of charge carriers and in some cases deteriorate the figure of merit zT. Isovalent substitution on the other hand can maintain charge-balance while enhancing phonon scattering.[7] Substitution of smaller atoms is of particular interest for a lower κ_L. If atoms are too small to fit into their sites, the weak bonding to surrounding atoms allows the central atom to move off its position. This off-centering can result in static disorder, or cause "rattling" if the atom shifts between equivalent positions, and is typically observed as high atomic displacement parameters or site splitting in the crystal structure. This is sometimes seen when atoms are doped into the vacant sites of skutterudites; the addition of Tl into Co_4Sb_{12} was observed to significantly reduce lattice thermal conductivity due to the resonant scattering of acoustic phonons by Tl rattlers.[8] Similarly, the framework structure of clathrates can cause off-centering or rattling of guest atoms in oversized cages which lowers thermal conductivity; these materials have significant interest for their thermoelectric potential.[9,10]

Zintl phases, with complex structures featuring a mix of electropositive metals and electronegative metalloids, are often narrow band gap semiconductors or semimetals.[11] This is due to transfer of electrons to form anionic metalloid species surrounded by cations, resulting in a charge-balanced material with a small band gap. Magnesium silicide (Mg_2Si) stands out

Special Issue: Dialogue on Zintl Chemistry

Received: March 15, 2024
Revised: June 24, 2024
Accepted: July 16, 2024

due to the high abundance and nontoxicity of its constituent elements. This cubic antifluorite structure compound has a narrow band gap and high-temperature operation potential, making it a prime candidate for optimizing lattice thermal conductivity through doping.[12−14] A notable example by V. K. Zaitsev et al. demonstrates this, where doping Mg_2Si with Sn anions enhanced its thermoelectric figure of merit from about 0.15 to 1.2 at 700 K.[15] Replacing magnesium with calcium yields Ca_2Si with the orthorhombic anti-$PbCl_2$ structure in space group *Pnma*; this compound exhibits semimetallic behavior. If one of the calcium sites is completely substituted by magnesium, this leads to CaMgSi with the TiNiSi structure type. CaMgSi is also semimetallic and has shown promising thermoelectric properties.[16] The synthesis of CaMgSi using Mg flux enables the formation of large crystals of this material.[17] A recent study of bulk CaMgSi and its off-stoichiometric $Ca_{1-x}Mg_{1+x}Si$ variants suggested that optimizing the Mg/Ca ratio could enhance the thermoelectric performance of these Zintl phases.[15]

More complex metal silicides can be formed by integrating heavier alkaline earth metals like barium. A variety of $(A/Mg)_2Si$ Zintl phases (with A = Ca, Sr, Ba, Eu, and Yb) were successfully grown as large crystals using Mg-based flux reactions.[18] These compounds maintain the charge-balanced 2:1 ratio of alkaline earth elements to silicon but exhibit more complex structure types. This is exemplified by $Ba_{1.9}Ca_{2.4}Mg_{9.7}Si_7$ which has a hexagonal $Zr_2Fe_{12}P_7$-type structure and promising thermoelectric properties, as evidenced by its zT of 0.35 at 900 K.[19] Similarly, $Ba_{20}Yb_{4.7}Mg_{61.3}Si_{43}$, $Ba_5Yb_{2.29}Mg_{16.71}Si_{12}$, $Ba_6Yb_{1.84}Mg_{18.16}Si_{13}$, and $Ba_2Yb_{0.88}Mg_{11.12}Si_7$ adopt $Ho_{20}Ni_{66}P_{43}$, $Ho_5Ni_{19}P_{12}$, $Ho_6Ni_{20}P_{13}$, and $Zr_2Fe_{12}P_7$-type hexagonal structures, respectively.[18] In these compounds, barium occupies the Ho (or Zr) sites; magnesium or Yb/Mg mixtures occupy the transition metal sites, and silicide anions occupy phosphorus sites. However, the effect of systematic mixing of atoms in specific crystallographic sites while maintaining the structure has not been investigated for this family of silicides.

In the present study, we reacted silicon with barium and strontium in a Mg-rich flux to grow a series of $(Ba/Sr)_{5+x}Mg_{19-x}Si_{12}$ Zintl phases as large crystals. These semimetallic compounds adopt the hexagonal $Ho_5Ni_{19}P_{12}$ structure type. As the Ba/Sr reactant ratio is changed, corresponding variations are seen in the occupancy of three specific crystallographic sites in the structure. Site mixing is anticipated to enhance phonon scattering and potentially reduce thermal conductivity; this was confirmed by measurements of the thermoelectric properties.

■ EXPERIMENTAL PROCEDURE

Synthesis. To carry out flux reactions, desired stoichiometric ratios of barium pieces (99.2%, Alfa Aesar) and strontium granules (99%, Beantown Chemical) were weighed and loaded into a niobium tube containing 22 mg of magnesium slug (99.95% Alfa Aesar), 8 mmol of zinc shot (99.99%, Alfa Aesar) and 3 mmol of silicon powder (99.9%, Beantown Chemical) in an argon-filled glovebox. The reaction ratios are listed in Table 1. The niobium crucible was welded shut in the argon-filled glovebox and then flame-sealed into quartz tubes under a vacuum. All reaction ampules were placed in a muffle furnace and heated from room temperature to 1323 K in 5 h, held at 1323 K for 10 h, cooled to 1023 K in 100 h, and held at 1023 K for 24 h, at which point the reaction ampules were quickly removed from the furnace, inverted, and centrifuged to remove excess flux. During this process, crystals adhere to the sides of one end of the niobium crucible. No filter was employed to separate the crystals from the molten flux. The crucibles were then cut open, and crystals of product were removed.

Table 1. Amounts of Ba and Sr (in Millimoles) Reacted with 3 mmol of Si in a Flux of 22:8 mmol Ratio of Mg/Zn; and the Corresponding Product Compositions from SC-XRD Analysis and SEM-EDS Elemental Analysis

Ba	Sr	Refined composition	Elemental Analysis
3	0	$Ba_5Mg_{19}Si_{12}$	$Ba_{4.6}Mg_{19}Si_{12.7}$
2.25	0.75	$Ba_{4.86}Sr_{2.94}Mg_{16.20}Si_{12}$	$Ba_{4.56}Sr_{2.76}Mg_{17.48}Si_{12}$
1.5	1.5	$Ba_{3.63}Sr_{4.20}Mg_{16.17}Si_{12}$	$Ba_{3.77}Sr_{4.23}Mg_{16}Si_{12}$
0.75	2.25	$Ba_{1.93}Sr_{5.99}Mg_{16.08}Si_{12}$	$Ba_{1.98}Sr_{5.88}Mg_{16.83}Si_{12}$
0	3	$Sr_{7.82}Mg_{16.18}Si_{12}$	$Sr_{7.6}Mg_{16.10}Si_{13.3}$

Elemental Analysis. SEM-EDS analyses were carried out using an FEI Nova 400 NanoSEM equipped with energy dispersive spectroscopy (EDS) capabilities. The crystal samples were mounted on aluminum pucks using carbon tape. To prevent any artifacts from the aluminum, the puck surfaces were entirely covered by the tape. The samples were analyzed using an acceleration voltage of 30 kV. Some regions of the crystal surfaces retained remnants of flux droplets, necessitating measurements to be conducted on either cleaved samples or areas free from flux. The resulting data on cleaved samples confirmed the absence of any zinc from the flux or elemental incorporation from the niobium crucible used in the process. The observed compositions are listed in Table 1.

Structural Characterization. The products were examined under an optical microscope, and tiny crystals with shiny surfaces were mounted on Hampton Cryoloop holders using Parabar oil. Single-crystal X-ray diffraction (SCXRD) data were collected by using a Rigaku XtaLAB Synergy-S diffractometer equipped with a Mo−Kα (λ = 0.7107 Å) source. Data were collected at room temperature, and the structure solution was determined by direct methods and refined using the SHELXTL program suite.[20,21] The structures of all of the $(Ba/Sr)_{5+x}Mg_{19-x}Si_{12}$ compounds were solved in the $Ho_5Ni_{19}P_{12}$ structure type in hexagonal space group $P\bar{6}2m$. All atoms were refined anisotropically. Due to being a light atom on a high symmetry special position surrounded by heavy atoms, the Mg on the 1a Wyckoff site on *(0,0,0)* exhibited unusual thermal parameters in all data sets. Face-indexing of the crystal and associated numerical absorption corrections were found to be effective in addressing this issue for the majority of the analogs studied, although the thermal ellipsoid for this site typically remains elongated along the *c*-axis. However, the $Ba_5Mg_{19}Si_{12}$ and $Sr_{7.82}Mg_{16.18}Si_{12}$ analogs still exhibited negative ADP values on this site and were therefore refined isotropically. Further crystallographic information for these compounds is shown in Table 2 and is also available as Crystallographic Information Files from the CCDC under the deposition numbers listed in the table.

Powder X-ray diffraction data were collected using a Rigaku SmartLab diffractometer (Cu Kα, λ = 1.54051 Å, 40 kV, 44 mA). Samples were ground to a fine powder using a mortar and pestle and placed on a small, zero-background sample holder. The scans were performed from 10° to 80° 2-theta, with a step size of 0.03° at 4 s per step.

Thermogravimetric Analysis/Differential Scanning Calorimetry. TGA-DSC measurements on a sample of $Ba_{3.63}Sr_{4.20}Mg_{16.17}Si_{12}$ were carried out using a TA Instruments Q600 SDT. The sample was heated to 1173 K at 10 K/min under flowing argon and then allowed to cool; data were collected during heating and cooling. PXRD data were collected on the sample after this process to investigate any resulting structural/composition changes.

Calculations of Electronic Structure. The electronic structures of $Ba_5Mg_{19}Si_{12}$ and $Sr_{7.82}Mg_{16.18}Si_{12}$ were investigated via DOS calculations employing Stuttgart TB-LMTO-ASA software. These computations drew from atomic coordinates and space groups obtained from single-crystal X-ray diffraction analyses.[22,23] To minimize the computing challenges of site mixing, we used ordered

Table 2. Crystallographic Data Collection Parameters for $(Ba/Sr)_{5+x}Mg_{19-x}Si_{12}$ Compounds

	$Ba_5Mg_{19}Si_{12}$	$Ba_{4.86}Sr_{2.94}Mg_{16.20}Si_{12}$	$Ba_{3.63}Sr_{4.20}Mg_{16.17}Si_{12}$	$Ba_{1.93}Sr_{5.99}Mg_{16.08}Si_{12}$	$Sr_{7.82}Mg_{16.18}Si_{12}$
M_r (g/mol)	1485.67	1655.98	1596.72	1517.89	1415.60
Crystal system	hexagonal				
Space group	$P\bar{6}2m$				
Temp (K)	297(2)				
a (Å)	14.6392(2)	14.9113(3)	14.9063(2)	14.8730(4)	14.8076(4)
c (Å)	4.47754(9)	4.5507(1)	4.5382(1)	4.5082(2)	4.4720(1)
V (Å^3)	831.00(3)	876.27(4)	873.28(3)	863.64(6)	849.18(5)
Z	1				
D_x (g/cm^3)	2.969	3.138	3.036	2.919	2.768
radiation	Mo Kα	Mo Kα	Mo Kα	Mo Kα	Mo Kα
μ (mm^{-1})	6.631	10.510	11.091	12.050	12.908
R_{int}	0.0509	0.0846	0.0691	0.1216	0.0570
limiting indices	$-23 < h < 24$	$-25 < h < 25$	$-25 < h < 25$	$-25 < h < 25$	$-23 < h < 22$
	$-23 < k < 23$	$-26 < k < 25$	$-25 < k < 25$	$-25 < k < 24$	$-22 < k < 23$
	$-7 < l < 7$	$-7 < l < 7$	$-7 < l < 7$	$-7 < l < 7$	$-7 < l < 7$
no. of reflections	1476	1828	1813	1762	1484
no. of parameters	45	47	48	48	45
GOF	1.123	1.119	1.090	1.050	1.107
R_1, wR_2 (all data)	0.0263, 0.0695	0.0268, 0.0477	0.0163, 0.0375	0.0370, 0.0720	0.0226, 0.0512
R_1, wR_2 ($I > 2\sigma(I)$)	0.0256, 0.0691	0.0230, 0.0470	0.0152, 0.0374	0.0305, 0.0700	0.0212, 0.0509
max peak, hole (e$^-$/Å^3)	5.700, −0.860	2.865, −1.146	1.953, −0.573	2.297, −0.983	2.260, −0.726
CCDC No.	2340498	2355286	2355287	2340494	2355176

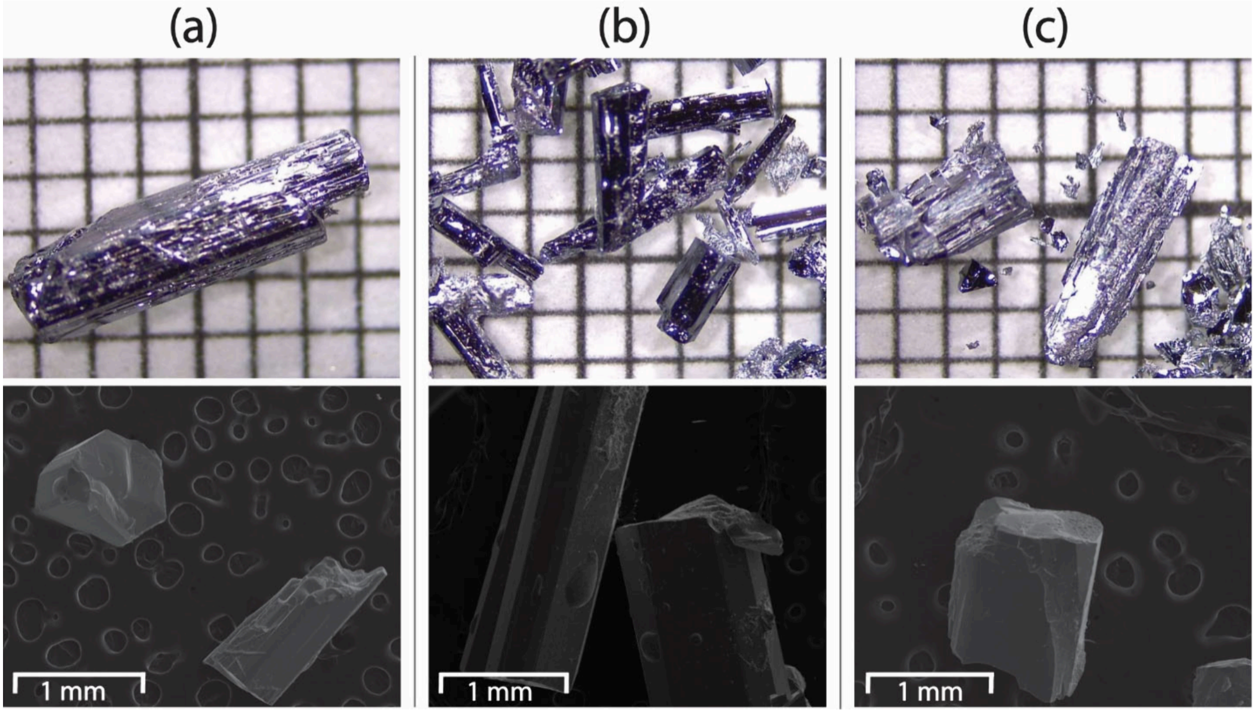

Figure 1. Optical microscopy images (top, on mm grid paper) and SEM images (bottom) of (a) $Ba_5Mg_{19}Si_{12}$, (b) $Ba_{3.63}Sr_{4.20}Mg_{16.17}Si_{12}$ and (c) $Sr_{7.82}Mg_{16.18}Si_{12}$ crystals.

models where the large atom positions (2*c* and 3*g* Wyckoff sites) were occupied by only one type of atom, and the small atom mixed site (3*f* Wyckoff site) was occupied by either Sr or Mg. The resulting model compounds are $Ba_5Mg_{19}Si_{12}$ and $Ba_8Mg_{16}Si_{12}$ (models for $Ba_5Mg_{19}Si_{12}$ crystal samples), and $Sr_5Mg_{19}Si_{12}$ and $Sr_8Mg_{16}Si_{12}$ (for $Sr_{7.82}Mg_{16.18}Si_{12}$). To fill the unit cell and address vacancies, we added empty spheres, where needed. An 18 × 18 × 6 k-point grid was used in these integrations, processed through the tetrahedron method. The orbital basis sets for these calculations consisted of 6s/6p/5d/4f for both Ba and Sr and 3s/3p/3d for Mg and Si. The orbitals Ba 6p, Sr 6p, Mg 3d, and Si 3d were downfolded to streamline the computation while maintaining the integrity of the electronic structure.

Thermoelectric Measurements of $Ba_5Mg_{19}Si_{12}$, $Sr_{7.82}Mg_{16.18}Si_{12}$ and $Ba_{3.63}Sr_{4.20}Mg_{16.17}Si_{12}$ Crystals. For the investigation of thermoelectric properties, single crystals were fashioned into bar shapes and affixed onto a specially designed holder with silver epoxy. This setup ensured alignment of both the electric current and the heat gradient with the long axis of the crystals (crystallographic *c*-axis). Thermal conductivity and Seebeck coefficients for the samples were determined using the classic one-heater-

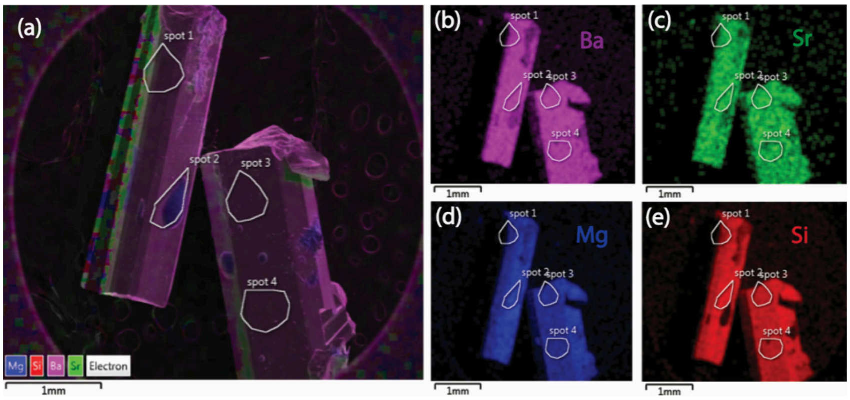

Figure 2. (a) SEM-EDX elemental mapping along with analysis of four random spots from a crystal of $Ba_{3.63}Sr_{4.20}Mg_{16.17}Si_{12}$ from reaction of Mg/Zn/Si/Ba/Sr at a millimolar proportion of 22:8:3:1.5:1.5; (b) elemental distributions of barium in purple, (c) strontium in green, (d) magnesium in blue, and (e) silicon in red.

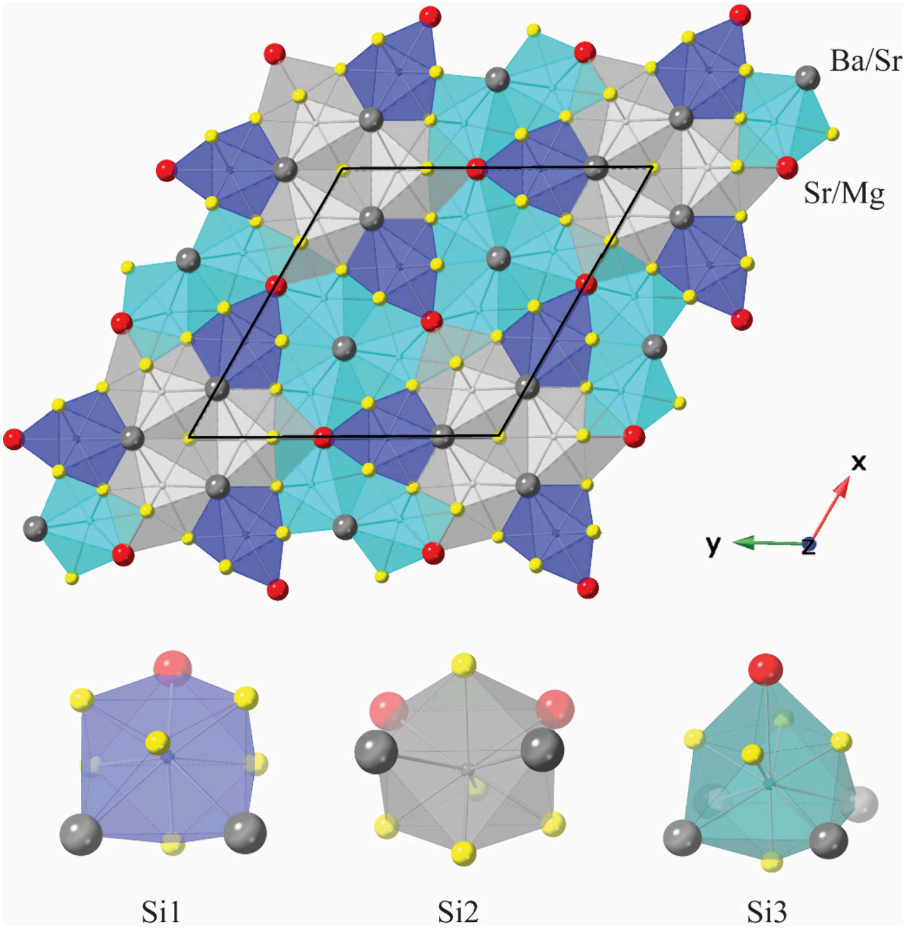

Figure 3. Structure of $Ba_{3.63}Sr_{4.20}Mg_{16.17}Si_{12}$. Structure is viewed down the *c*-axis, with coordination of three different silicide anions shown as blue, silver, and cyan polyhedra. Tricapped trigonal prismatic coordination of the three different silicide sites viewed perpendicular to the long trigonal prism axis. Ba/Sr mixed sites (2*c* and 3*g* sites) shown in gray, Sr/Mg (3*f* site) in red, and Mg sites as yellow spheres.

two-thermometer technique. We utilized two Cernox sensors as thermometers and a refined, polished metallic chip as the heating element. Incremental power was supplied to the heater, inducing stepwise thermal gradients through the specimens. The resulting temperature differences and thermoelectric voltages were recorded concurrently once the system reached thermal equilibrium at each power increment. Separately, electrical resistivity was measured on the same crystals using a four-wire configuration within a Quantum Design Physical Property Measurement System (PPMS) in the temperature range from 1.8 to 400 K.

■ RESULTS AND DISCUSSION

Synthesis. Silicon was reacted with barium and/or strontium in excess of a flux comprised of magnesium and zinc. The Mg/Zn phase diagram has a eutectic point at a ratio of 72:28 at. % which melts at around 614 K. Zinc effectively lowers the melting point and viscosity of magnesium, thus optimizing the reaction conditions and crystal growth as well as facilitating the removal of the flux by centrifugation. Zinc

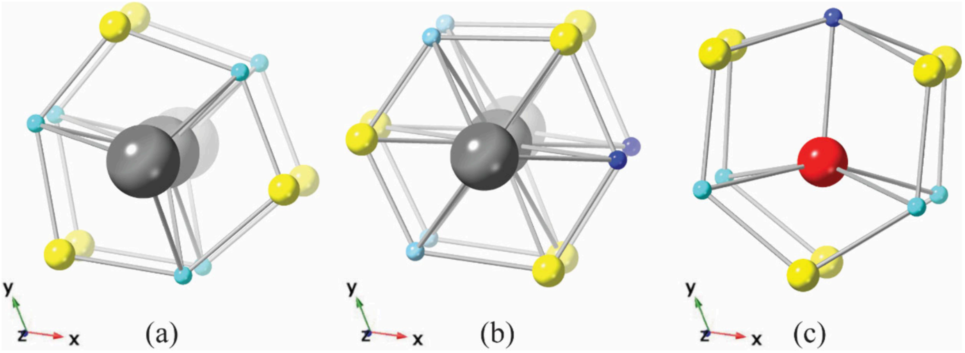

Figure 4. Coordination environments of two unique Ba/Sr mixed sites in the (a) 2*c* site, (b) 3*g* site, and (c) Sr/Mg 3*f* site in $(Ba/Sr)_{5+x}Mg_{19-x}Si_{12}$ compounds viewed along the *c*-axis.

Table 3. Comparison of Mixed Site Occupancies and Bond Lengths around the Ba and Sr Sites in the $(Ba/Sr)_{5+x}Mg_{19-x}Si_{12}$ Compounds

	$Ba_5Mg_{19}Si_{12}$	$Ba_{4.86}Sr_{2.94}Mg_{16.20}Si_{12}$	$Ba_{3.63}Sr_{4.20}Mg_{16.17}Si_{12}$	$Ba_{1.93}Sr_{5.99}Mg_{16.08}Si_{12}$	$Sr_{7.82}Mg_{16.18}Si_{12}$
2*c* site occupancy	100% Ba	100% Ba	70.0(8)% Ba/30.0(8)% Sr	44(1)% Ba/56(1)% Sr	100% Sr
3*g* site occupancy	100% Ba	95.0(8)% Ba/5.0(8)% Sr	77.0(7)% Ba/23.0(7)% Sr	35(1)% Ba/65(1)% Sr	100% Sr
3*f* site occupancy	100% Mg	93.0(6)% Sr/7.0(6)% Mg	94.0(5)% Sr/6.0(5)% Mg	97.0(8)% Sr/3.0(8)% Mg	94(6)% Sr/6.0(6)% Mg
2*c* site - Si	3.442(2) Å× 6	3.5028(9) Å × 6	3.4958(6) Å × 6	3.471(1) Å × 6	3.4337(7) Å × 6
2*c* site - Mg	3.652(2) Å× 6	3.723(1) Å × 6	3.7193(9) Å × 6	3.711(2) Å × 6	3.687(1) Å × 6
3*g* site - Si	3.471(1) Å× 2	3.515(2) Å × 2	3.502(1) Å × 2	3.475(2) Å × 2	3.448(1) Å × 2
	3.504(2) Å × 4	3.5269(7) Å × 4	3.5153(5) Å × 4	3.4924(8) Å × 4	3.4592(6) Å × 4
3*g* site - Mg	3.5303(4) Å × 2	3.5754(3) Å × 2	3.5625(2) Å × 2	3.5380(5) Å × 2	3.5008(4) Å × 2
	3.604(3) Å × 2	3.598(2) Å × 2	3.591(1) Å × 2	3.579(2) Å × 2	3.569(2) Å × 2
	3.611(3) Å × 2	3.624(1) Å × 2	3.619(1) Å × 2	3.610(2) Å × 2	3.605(1) Å × 2
3*f* site - Si		3.040(2) Å × 1	3.052(1) Å × 1	3.052(2) Å × 1	3.040(2) Å × 1
		3.2410(9) Å × 4	3.237(1) Å × 4	3.227(1) Å × 4	3.2077(8) Å × 4
3*f* site - Mg		3.255(2) Å × 2	3.263(1) Å × 2	3.271(2) Å × 2	3.261(2) Å × 2
		3.281(2) Å × 2	3.287(1) Å × 2	3.290(2) Å × 2	3.281(2) Å × 2
		3.542(1) Å × 3	3.538(1) Å × 3	3.520(2) Å × 3	3.494(1) Å × 3

functions as an inert solvent component, akin to the role of aluminum in similar Mg/Al flux systems studied in our group.[19] It is notable that pure magnesium is not effective as a flux compared to Mg/Zn.[24] The large amount of magnesium in the flux promotes the formation of magnesium-rich products. This likely prevents the formation of known AMgTt phases with the orthorhombic TiNiSi structure type; for instance, SrMgSi or BaMgSi is not seen.[24] Instead, the reactions reported here yield $(Ba/Sr)_{5+x}Mg_{19-x}Si_{12}$ products with the hexagonal $Ho_5Ni_{19}P_{12}$ structure type. Thermal analysis (TGA/DSC under argon) suggests that they remain stable up to 1173 K; the PXRD analysis of samples before and after heating to this temperature revealed no decomposition or change in structure (see Supporting Information, Figure S2). Very minor peaks around 873 K in the DSC data for $Ba_{3.63}Sr_{4.20}Mg_{16.17}Si_{12}$ can be attributed to the melting/freezing of residual flux on the specimen. Droplets of flux residue were observed on the crystal surfaces by SEM-EDX analysis of selected crystals (Figure 1). These $(Ba/Sr)_{5+x}Mg_{19-x}Si_{12}$ compounds exhibit significant resistance to oxidation, even after being exposed to air for multiple weeks, but will dissolve in 1 M HCl. To test the oxidation resistance, $Ba_{3.63}Sr_{4.20}Mg_{16.17}Si_{12}$ crystals were ground to powder and exposed to air for over a year without degradation. Identical PXRD patterns of the aged powders compared to fresh samples confirm their stability (Figure S3).

For the most part, the composition of the products displayed the expected dependence on the initial Ba/Sr reactant ratios (Table 1), highlighting the ability to control product composition of flux reactions in the Mg/Zn medium. $Ba_5Mg_{19}Si_{12}$ is formed in reactions with only barium present to react with silicon (Ba/Sr of 3:0). The other end-member $Sr_{7.82}Mg_{16.18}Si_{12}$ is formed at a Ba:Sr ratio of 0:3. For reactions using both barium and strontium, Ba/Sr reactant ratios are close to those seen in the composition of the product. For example, with an equimolar Ba/Sr reactant ratio (1.5:1.5), the resulting $Ba_{3.63}Sr_{4.20}Mg_{16.17}Si_{12}$ product has almost equal amounts of barium and strontium, although a slight preference for Sr is observed. SEM-EDX elemental mapping of crystals of this compound (Figure 2) revealed a consistent elemental distribution across various sample spots; this indicates a homogeneous distribution of Ba and Sr across the sample rather than clustering of the elements into different regions. The atomic percentages indicated by EDX are consistent with those obtained through single crystal X-ray diffraction (SCXRD) refinement of $(Ba/Sr)_{5+x}Mg_{19-x}Si_{12}$ samples, as evidenced by Figures S4–S7 and Table S1.

Structure. The $(Ba/Sr)_{5+x}Mg_{19-x}Si_{12}$ compounds listed in Table 1 have the $Ho_5Ni_{19}P_{12}$ structure in the hexagonal space group $P\bar{6}2m$. The formulae have 24 divalent cations (Ba^{2+}/Sr^{2+}/Mg^{2+}) and 12 silicide anions (Si^{4-}); the compounds are therefore charge-balanced Zintl phases. The formation of only $Ho_5Ni_{19}P_{12}$-type structures, rather than the related $Zr_2Fe_{12}P_7$-type or $Ho_{20}Ni_{66}P_{43}$-type, is notable and may indicate that the latter two structures are less stable under the reaction

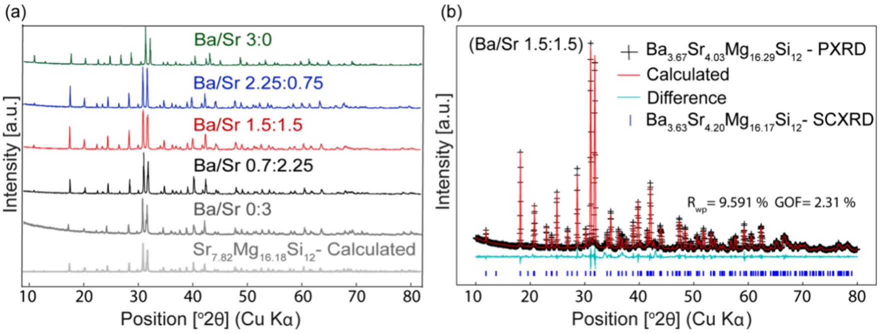

Figure 5. (a) Powder X-ray diffraction data for five $(Ba/Sr)_{5+x}Mg_{19-x}Si_{12}$ products grown in Mg/Zn flux, compared to calculated powder pattern for $Sr_{7.82}Mg_{16.18}Si_{12}$ (bottom pattern) based on single crystal data. (b) GSAS-II refinement of powder XRD data for $Ba_{3.63}Sr_{4.20}Mg_{16.17}Si_{12}$.

conditions used. The $Ho_5Ni_{19}P_{12}$ parent structure has three crystallographically unique phosphorus sites, two unique holmium sites, and five unique nickel sites. All of the phosphorus sites are occupied by silicon in the title compounds. The holmium sites (2*c* and 3*g* Wyckoff sites) are occupied by either barium, strontium, or a Ba/Sr mixture. Four of the five nickel sites are completely occupied by magnesium. The fifth nickel site (3*f* Wyckoff site) can incorporate a mixture of magnesium and strontium. The structure is shown in Figure 3.

In the context of thermoelectric properties, having a mixture of cations in a crystallographic site promotes phonon scattering through disorder within the unit cell.[19,25] The $(Ba/Sr)_{5+x}Mg_{19-x}Si_{12}$ analogs have possible cation mixing on three sites in the structure (Ba/Sr mixing on the 2*c* and 3*g* sites, and Sr/Mg mixing on the 3*f* site) which are shown in Figure 4. Because of this extensive mixing on multiple sites, Vegard's law is not followed in this series of compounds. In $Ba_5Mg_{19}Si_{12}$, the 2*c* and 3*g* sites are fully occupied by barium; barium does *not* mix on the 3*f* site, in accordance with the significantly larger radius of Ba^{2+} compared to that of Mg^{2+}. For $Sr_{7.82}Mg_{16.18}Si_{12}$, the strontium not only fully occupies the 2*c* and 3*g* sites but also dominates the 3*f* sites (Sr/Mg, 94%/6% mixing on this site). In $Ba_{3.63}Sr_{4.20}Mg_{16.17}Si_{12}$, the 2*c* and 3*g* sites exhibit mixed Ba/Sr occupancies (Ba/Sr percentages of 70%/30% in 2*c*, and 77%/23% in 3*g*). The 3*f* site is occupied by Sr/Mg, 94%/6% (see Table 3).

In the endmember $Ba_5Mg_{19}Si_{12}$, the bond lengths between barium and silicon fall within the range 3.442(2)−3.503(4) Å (detailed in Table 3). This is similar to Ba−Si distances seen in binary compounds Ba_2Si and $BaSi_2$, which range from 3.25 to 3.63 Å.[26,27] Another binary Ba/Si compound of particular interest is the clathrate phase Ba_8Si_{46}. Clathrate structures are characterized by frameworks that create cages around cations; in some cases, these cages are too large to accommodate the size of the cation, which then rattles. This aids in scattering phonons and lowering the thermal conductivity. For Ba_8Si_{46}, a wide range of Ba−Si distances from 3.33 to 3.97 Å is seen.[28] The relatively uniform and shorter Ba−Si bond lengths in $Ba_5Mg_{19}Si_{12}$ suggest a more consistent local environment for Ba atoms, possibly due to a more rigid and less spacious structural arrangement compared to the clathrate's cage-like structure.[29]

In the strontium endmember $Sr_{7.82}Mg_{16.18}Si_{12}$, the Sr−Si bond distances range from 3.4337(7) Å and 3.4592(6) Å in the 2*c* and 3*g* sites, respectively. The Sr−Si distances in the binary compound Sr_2Si are reported to be between 3.16 and 3.26 Å,[30] and the distances in $SrSi_2$ range from 3.19 to 3.35 Å.[31] This highlights the slightly too large Sr−Si distance in $Sr_{7.82}Mg_{16.18}Si_{12}$, which might result in rattling of Sr cations. The 3*f* site in this compound has a mixed occupancy of Sr/Mg, with a (Sr/Mg)−Si distance of 3.040(2)−3.2077(8) Å.

In Ba/Sr mixed samples, where Ba/Sr are cooccupying 2*c* and 3*g* sites, and Sr is mixing on the 3*f* site, the observed (Ba/Sr)-Si distance is even larger than that of Ba-rich and Sr-rich samples. The presence of barium mixing in the 2*c* and 3*g* sites, along with strontium mixing in the 3*f* site, serves to expand the structure, leading to overall larger unit cell volumes and longer (Ba/Sr)−Si bonds. In $Ba_{3.63}Sr_{4.20}Mg_{16.17}Si_{12}$, (Ba/Sr)−Si bond distances of 3.4958(6)−3.5153(5) Å are observed, which are notably larger than those in the individual Ba-rich ($Ba_5Mg_{19}Si_{12}$) and Sr-rich ($Sr_{7.82}Mg_{16.18}Si_{12}$) compounds. This increase in bond lengths within the Ba/Sr mixed samples may lead to increased rattling of the heavy Ba and Sr atoms; a decrease in the lattice thermal conductivity can be expected.

Despite the incorporation of four elements, complex structure with multiple site mixing, and a high number of possible competing binary and ternary products, PXRD data indicate that the solids obtained from each reaction are essentially single phase $(Ba/Sr)_{5+x}Mg_{19-x}Si_{12}$. The resulting powder patterns are shown in Figure 5; all of the data sets correspond to the $Ho_5Ni_{19}P_{12}$ structure type. The intensities of several of the peaks change notably as lighter Sr is substituted with heavier Ba in the mixed sites. Rietveld analysis was carried out on the product of the reaction with equimolar amounts of strontium and barium (1.5 mmol each); these data are compared to the pattern calculated from the single crystal data of $Ba_{3.63}Sr_{4.20}Mg_{16.17}Si_{12}$. The Rietveld analysis of the powder pattern indicated unit cell parameters a = 14.908(1) Å and c = 4.547(2) Å, which corresponds closely with the lattice parameters from single crystal data. Refinement of the occupancies in mixed sites (Table S2, Supporting Information) shows that the 2*c* site is occupied by Ba/Sr at a 78%/22% ratio, the 3*g* site is occupied by Ba/Sr at 70%/30%, and the 3*f* site is occupied by Sr/Mg at 90%/10%. This yields an overall composition of $Ba_{3.67}Sr_{4.03}Mg_{16.29}Si_{12}$. This is in good agreement with the $Ba_{3.68}Sr_{4.07}Mg_{16.24}Si_{12}$ stoichiometry indicated by refinement of single crystal data (see Table 3).

Electronic Structure and Transport Properties. To better understand the electronic properties of $(Ba/Sr)_{5+x}Mg_{19-x}Si_{12}$ materials, Density of States (DOS) calculations were carried out on four model compounds $Ba_5Mg_{19}Si_{12}$, $Ba_8Mg_{16}Si_{12}$, $Sr_5Mg_{19}Si_{12}$, and $Sr_8Mg_{16}Si_{12}$. This was achieved by substituting Ba or Sr for Mg in the 3*f* Wyckoff sites in the crystal structure, transforming $Ba_5Mg_{19}Si_{12}$ into $Ba_8Mg_{16}Si_{12}$ and $Sr_5Mg_{19}Si_{12}$ into $Sr_8Mg_{16}Si_{12}$.

https://doi.org/10.1021/acs.inorgchem.4c01079
Inorg. Chem. XXXX, XXX, XXX−XXX

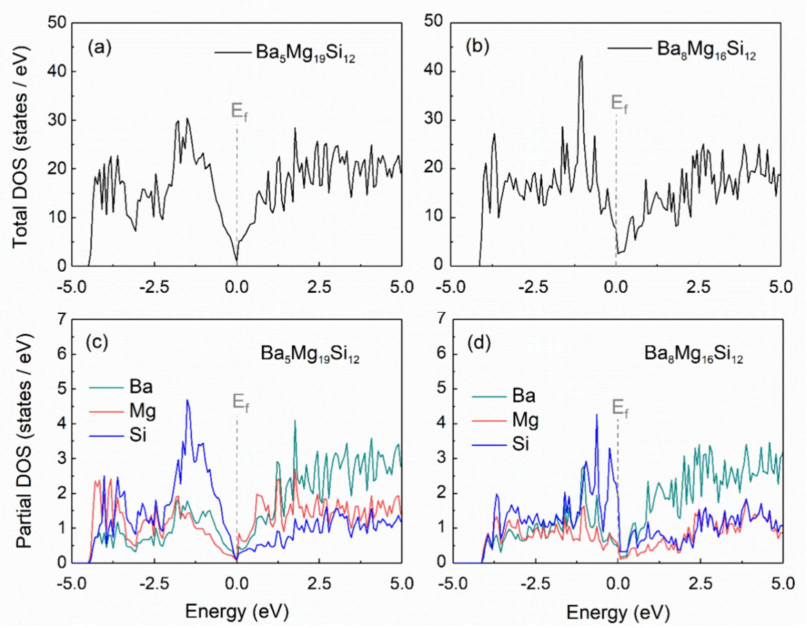

Figure 6. Density of states data for (a) $Ba_5Mg_{19}Si_{12}$ and (b) $Ba_8Mg_{16}Si_{12}$. The E_F is set to 0 eV. Corresponding partial density of states contributions for Ba, Mg and Si elements are shown for (c) $Ba_5Mg_{19}Si_{12}$ and (d) $Ba_8Mg_{16}Si_{12}$.

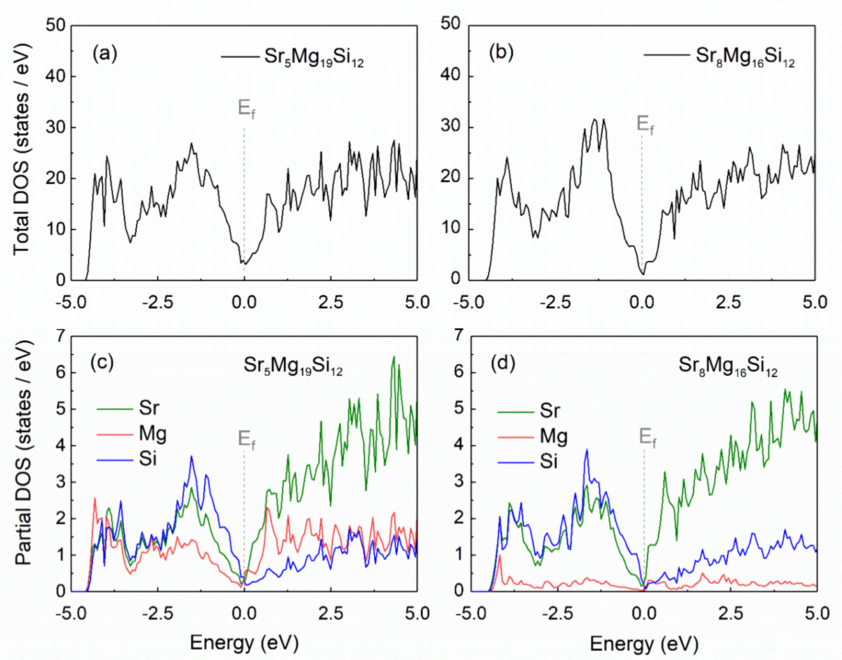

Figure 7. Density of states data for (a) $Sr_5Mg_{19}Si_{12}$ and (b) $Sr_8Mg_{16}Si_{12}$. The E_F is set to 0 eV. Corresponding partial density of states contributions for Sr, Mg and Si elements are shown for (c) $Sr_5Mg_{19}Si_{12}$ and (d) $Sr_8Mg_{16}Si_{12}$.

As shown in Figure 6 and Figure 7, all models exhibit a pseudogap at the Fermi level. This is in agreement with the charge-balanced nature of these Zintl phases.[32,33] The low (but nonzero) density of states at E_F is characteristic of semimetals. The fact that there are some states at the Fermi level means that there are available energy states for electrons to occupy, but the number of carriers will not be as high as a typical metal, which will lead to lower conductivity compared to a metal. The partial density of states data show that silicon states dominate the contribution to valence bands below the Fermi level, while alkaline earth metal states dominate conduction bands above E_F; this is in agreement with formation of silicide anions and metal cations. Comparison between $Ba_5Mg_{19}Si_{12}$ and $Ba_8Mg_{16}Si_{12}$ indicates that the latter has more states at E_F and should therefore be a better metal with higher conductivity. However, the refined single crystal data indicated a composition closer to that of the $Ba_5Mg_{19}Si_{12}$ model. For the strontium models (depicted in Figure 7) the increased Sr content of $Sr_8Mg_{16}Si_{12}$ slightly decreases the pseudogap at the Fermi level in the DOS, suggesting slightly more metallic character compared to $Sr_5Mg_{19}Si_{12}$, but not as high as a typical metal. This suggests that the observed analogue $Sr_{7.84}Mg_{16.16}Si_{12}$ is likely a poor metal, with conduction facilitated by the empty strontium states just above the

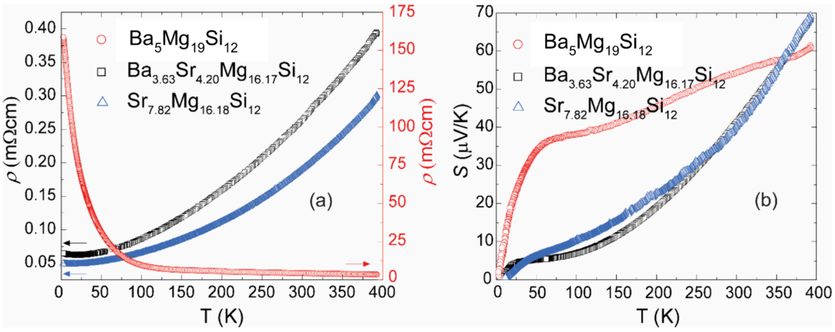

Figure 8. Temperature dependent (a) electrical resistivity ρ, and (b) Seebeck coefficient, S, for $Ba_5Mg_{19}Si_{12}$, $Ba_{3.63}Sr_{4.20}Mg_{16.17}Si_{12}$, and $Sr_{7.82}Mg_{16.18}Si_{12}$. Note the change in scale for resistivity (data for $Ba_5Mg_{19}Si_{12}$ are colored red, with values on the secondary axis).

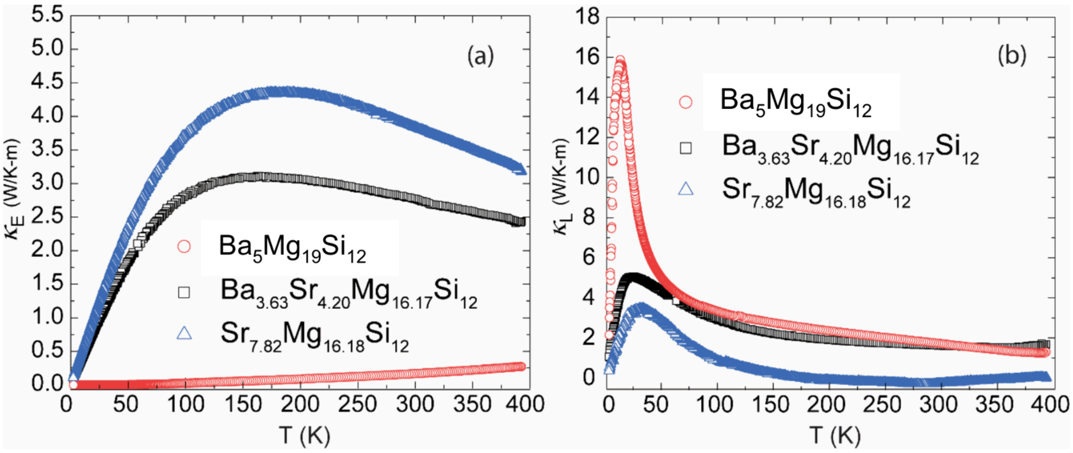

Figure 9. Temperature dependent (a) electronic thermal conductivity κ_E, and (b) lattice thermal conductivity κ_L for $Ba_5Mg_{19}Si_{12}$, $Ba_{3.63}Sr_{4.20}Mg_{16.17}Si_{12}$, and $Sr_{7.82}Mg_{16.18}Si_{12}$.

Fermi level. While the mixed cation $(Ba/Sr)_{5+x}Mg_{19\text{-}x}Si_{12}$ phases could not be modeled, their likely behavior can be extrapolated from that of the end members. Due to their charge-balanced Zintl phase nature and identical structure, they are likely to have a pseudogap at the Fermi level, but the depth of this gap may be influenced by the relative proportions of Ba and Sr.

Thermoelectric Properties of $Ba_5Mg_{19}Si_{12}$, $Sr_{7.82}Mg_{16.18}Si_{12}$, and $Ba_{3.63}Sr_{4.20}Mg_{16.17}Si_{12}$. The thermoelectric properties of three analogs were measured. Figure 8a illustrates the electrical resistivity (ρ) as a function of temperature (T) for single crystals of the Ba-analog, Sr-analog, and $Ba_{3.63}Sr_{4.20}Mg_{16.17}Si_{12}$. The barium endmember $Ba_5Mg_{19}Si_{12}$ demonstrates a pronounced semiconductor-like behavior, consistent with prior reports.[24] Fitting of these resistivity data using the Arrhenius equation indicates a very small intrinsic band gap of 2.2×10^{-2} eV (Figure S9). The extremely small band gap and semiconductor behavior indicate that the DOS calculations underestimate the band gap as they show a pseudogap with the presence of some (but not zero) electronic states at the Fermi level.

The other two analogs have resistivity orders of magnitude smaller, and both exhibit resistivity increasing with temperature. These behaviors indicate that $Sr_{7.82}Mg_{16.18}Si_{12}$ and $Ba_{3.63}Sr_{4.20}Mg_{16.17}Si_{12}$ are poor metals. The increased structural disorder of the strontium analogs (with Sr/Mg mixing on the $3f$ site in both) and the broader bands of the heavier elements may lead to the metallic behavior seen in Figure 8a. $Ba_5Mg_{19}Si_{12}$ on the other hand is well-ordered (100% Ba in the $2c$ and $3g$ sites; 100% Mg in the $3f$ sites) and more magnesium-rich.

The Seebeck coefficient behavior, depicted in Figure 8b, shows positive values of S rising to around 60 μV/K at 350 K for all three compounds, indicating that they are p-type materials. $Ba_5Mg_{19}Si_{12}$ shows a steep initial increase up to 50 K and then a more gradual rise up to room temperature. In contrast, the Sr-containing samples have a slight peak at much lower temperatures (~35 K) with substantially lower values than the barium analog. However, the $Sr_{7.82}Mg_{16.18}Si_{12}$ and $Ba_{3.63}Sr_{4.20}Mg_{16.17}Si_{12}$ samples outperform the barium compound in S at temperatures above 350 K. This suggests that Sr not only contributes to reduced electrical resistivity but also enhances the Seebeck coefficient at higher temperatures, which may be due to the altered band structure in these samples.

Figure 9a and Figure 9b show the electronic (κ_E) and lattice (κ_L) thermal conductivities. The electronic thermal conductivity depends on the resistivity as expected, being calculated from ρ using Wiedemann–Franz law ($\kappa/\sigma = LT$),[34] with the metallic compounds $Sr_{7.82}Mg_{16.18}Si_{12}$ and $Ba_{3.63}Sr_{4.20}Mg_{16.17}Si_{12}$ showing high κ_E and the semiconducting $Ba_5Mg_{19}Si_{12}$ having a much lower value. The lattice thermal conductivity clearly shows the impact of increasing disorder. The barium analogue has the highest κ_L; while it contains heavy barium ions, they are ordered within their sites in the structure. The strontium-containing materials, with multiple mixed sites, have lower κ_L. It is somewhat surprising that $Sr_{7.82}Mg_{16.18}Si_{12}$ has a lower thermal conductivity than the far more disordered $Ba_{3.63}Sr_{4.20}Mg_{16.17}Si_{12}$. This may indicate that the smaller strontium cations have a greater tendency to rattle, leading to vibrational states that disrupt acoustic phonon transport, in comparison to the larger barium ions. This will enhance the thermoelectric performance without impeding electrical conductivity. All three compounds exhibit the expected peak at low temperatures which is due to the decrease in lattice vibrations as the temperature drops (which leads to an increase in κ_L) intersecting with the typical T^3 temperature dependence at very low temperatures.[35,36]

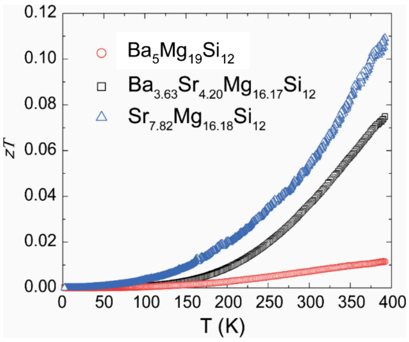

Figure 10. Dimensionless figure of merit zT as a function of the temperature for $Ba_5Mg_{19}Si_{12}$, $Ba_{3.63}Sr_{4.20}Mg_{16.17}Si_{12}$, and $Sr_{7.82}Mg_{16.18}Si_{12}$.

Finally, Figure 10 illustrates the dimensionless figure of merit, $zT = \frac{S^2\sigma}{\kappa}T$, across all three samples. Notably, while $Sr_{7.82}Mg_{16.18}Si_{12}$ did not exhibit the highest Seebeck coefficient (S) values below 350 K, it has the highest zT value across the entire measurement range ($1.8 \text{ K} < T < 400 \text{ K}$). This is largely attributable to the lattice contribution to thermal conductivity (κ_L), where this compound demonstrated the lowest value among the three materials studied. This can be ascribed to the rattling effect induced by the Sr ions, as previously discussed. While the zT value is a relatively modest 0.11 at 400 K, it is likely to rise with temperature. Comparison can be made to $Ba_{1.9}Ca_{2.4}Mg_{9.7}Si_7$; this was also grown in Mg-based flux and has the $Zr_2Fe_{12}P_7$-type structure, which is simpler than the $Ho_5Ni_{19}Si_{12}$ structure type exhibited by the $(Ba/Sr)_{5+x}Mg_{19-x}Si_{12}$ phases studied here.[17] At 400 K, $Ba_{1.9}Ca_{2.4}Mg_{9.7}Si_7$ has a Seebeck coefficient of −70 μV/K and a zT of 0.025; these values rise with temperature to values of S = −175 μV/K and zT = 0.35 at 900 K.[19] The behavior of $Sr_{7.82}Mg_{16.18}Si_{12}$ at 400 K (S = 70 μV/K and zT = 0.11) indicates that its high temperature thermoelectric properties should be more impressive; further studies are needed.

CONCLUSIONS

In this work, we synthesized a series of $(Ba/Sr)_{5+x}Mg_{19-x}Si_{12}$ Zintl phases using Mg/Zn flux to investigate the role of the crystallographic site mixing in modulating structural and thermoelectric properties. The flux reactions enabled isolation of single phase products with targeted compositions, which is remarkable considering the number of possible binary and ternary competing phases. Varying the Ba/Sr ratio affects the occupancy of three sites in the structure that are amenable to Ba/Sr/Mg cation mixing. Compared to the ordered $Ba_5Mg_{19}Si_{12}$ analogue (which has no site mixing), introduction of Sr onto these three sites induces changes in the unit cell parameter and positions strontium atoms in sites that are too large. The incorporation of Sr increased electrical conductivity while it reduced the thermal conductivity. This leads to improved thermoelectric properties seen for $Ba_{3.63}Sr_{4.20}Mg_{16.17}Si_{12}$ and $Sr_{7.82}Mg_{16.18}Si_{12}$ when compared with those of $Ba_5Mg_{19}Si_{12}$. Our findings suggest that substitution of smaller cations into the structure impacts the figure of merit zT by lowering the thermal conductivity, possibly due to rattling or off-centering of the Sr^{2+} cations, akin to what has been observed in clathrates such as $Sr_8Ga_{16}Ge_{30}$.[37] Additional characterization of the positions and thermal parameters of the Sr atoms at low temperature is needed to shed light on this. Preliminary SC-XRD data collected on $Sr_{7.82}Mg_{16.18}Si_{12}$ at 100 K show some evidence of site splitting for two of the Sr sites. Moreover, such findings strongly suggest that exploring the substitution of even smaller cations such as calcium or ytterbium into the highly flexible $(Ba/Sr)_{5+x}Mg_{19-x}Si_{12}$ structure could yield further enhancements in zT.

ASSOCIATED CONTENT

Supporting Information

The Supporting Information is available free of charge at https://pubs.acs.org/doi/10.1021/acs.inorgchem.4c01079.

> Optical microscopy for several $(Ba/Sr)_{5+x}Mg_{19-x}Si_{12}$ compounds, SEM-EDS images and EDX mapping of $(Ba/Sr)_{5+x}Mg_{19-x}Si_{12}$ samples, DSC/TGA data, comparison of powder XRD patterns for aged ground crystals $Ba_{3.63}Sr_{4.20}Mg_{16.17}Si_{12}$ with the as-synthesized sample, PXRD data and Rietveld analysis of $(Ba/Sr)_{5+x}Mg_{19-x}Si_{12}$ compounds, atomic positions for $(Ba/Sr)_{5+x}Mg_{19-x}Si_{12}$ compounds, Arrhenius plot for $Ba_5Mg_{19}Si_{12}$ (PDF)

Accession Codes

CCDC 2340494, 2340498, 2355176, and 2355286−2355287 contain the supplementary crystallographic data for this paper. These data can be obtained free of charge via www.ccdc.cam.ac.uk/data_request/cif, or by emailing data_request@ccdc.cam.ac.uk, or by contacting The Cambridge Crystallographic Data Centre, 12 Union Road, Cambridge CB2 1EZ, UK; fax: +44 1223 336033.

AUTHOR INFORMATION

Corresponding Author

Susan E. Latturner − *Department of Chemistry and Biochemistry, Florida State University, Tallahassee, Florida 32306, United States;* orcid.org/0000-0002-6146-5333; Email: slatturner@fsu.edu

Authors

Amirhossein Zareihassangheshlaghi − *Department of Chemistry and Biochemistry, Florida State University, Tallahassee, Florida 32306, United States*

Jorge Galeano-Cabral − *National High Magnetic Field Laboratory, Tallahassee, Florida 32310, United States*

Md Sahab Uddin − *Department of Chemistry and Biochemistry, Florida State University, Tallahassee, Florida 32306, United States*

Benny Schundelmier − *National High Magnetic Field Laboratory, Tallahassee, Florida 32310, United States;* orcid.org/0000-0002-7345-9977

Kaya Wei − *National High Magnetic Field Laboratory, Tallahassee, Florida 32310, United States*

Ryan E. Baumbach – *National High Magnetic Field Laboratory, Tallahassee, Florida 32310, United States*

Complete contact information is available at:
https://pubs.acs.org/10.1021/acs.inorgchem.4c01079

Notes

The authors declare no competing financial interest.

■ ACKNOWLEDGMENTS

This research was supported by the Division of Materials Research of the National Science Foundation (DMR-2126077). We also acknowledge the FSU X-ray Characterization Center (FSU075000XRAY), an integral part of the Department of Chemistry and Biochemistry at Florida State University, for providing the necessary facilities for this research. Special thanks are extended to Dr. Xinsong Lin for his invaluable technical assistance and expertise with the X-ray equipment. The thermoelectric properties measurements undertaken in this study were supported by the National High Magnetic Field Laboratory, which is supported by the National Science Foundation through NSF/DMR-2128556 and NSF/DMR-1644779, and the State of Florida. We are also grateful for the access to the advanced scanning electron microscopy facilities at the Florida State University's Department of Biology's Biological Sciences Imaging Resource (BSIR). Our appreciation extends to Dr. Eric Lochner, whose assistance and technical guidance were crucial to our analyses.

■ REFERENCES

(1) Snyder, G. J.; Toberer, E. S. Complex Thermoelectric Materials. *Nat. Mater.* **2008**, *7* (2), 105–114.

(2) Yan, Q.; Kanatzidis, M. G. High-Performance Thermoelectrics and Challenges for Practical Devices. *Nat. Mater.* **2022**, *21* (5), 503–513.

(3) Biswas, K.; He, J.; Blum, I. D.; Wu, C.-I.; Hogan, T. P.; Seidman, D. N.; Dravid, V. P.; Kanatzidis, M. G. High-Performance Bulk Thermoelectrics with All-Scale Hierarchical Architectures. *Nature* **2012**, *489* (7416), 414–418.

(4) Hu, C.; Xia, K.; Fu, C.; Zhao, X.; Zhu, T. Carrier Grain Boundary Scattering in Thermoelectric Materials. *Energy Environ. Sci.* **2022**, *15* (4), 1406–1422.

(5) Li, M.; Wuliji, H.; Zhou, Z.; Qiu, P.; Zhao, K.; Shi, X. Co-Alloying of Sn and Te Enables High Thermoelectric Performance in Ag_9GaSe_6. *J. Mater. Chem. A* **2023**, *11* (20), 10901–10911.

(6) Li, J.-F.; Liu, W.-S.; Zhao, L.-D.; Zhou, M. High-Performance Nanostructured Thermoelectric Materials. *NPG Asia Mater.* **2010**, *2* (4), 152–158.

(7) *Chemistry, Structure, and Bonding of Zintl Phases and Ions*; Kauzlarich, S. M., Ed.; The chemistry of metal clusters; VCH: New York, NY, 1996.

(8) Sales, B. C.; Chakoumakos, B. C.; Mandrus, D. Thermoelectric Properties of Thallium-Filled Skutterudites. *Phys. Rev. B* **2000**, *61* (4), 2475–2481.

(9) Dolyniuk, J.-A.; Owens-Baird, B.; Wang, J.; Zaikina, J. V.; Kovnir, K. Clathrate Thermoelectrics. *Mater. Sci. Eng. R Rep.* **2016**, *108*, 1–46.

(10) Nolas, G. S.; Slack, G. A.; Schujman, S. B. Chapter 6 Semiconductor Clathrates: A Phonon Glass Electron Crystal Material with Potential for Thermoelectric Applications. In *Recent Trends in Thermoelectric Materials Research I*; Tritt, T. M., Ed.; Semiconductors and Semimetals; Elsevier, 2001; Vol. *69*, pp 255–300. DOI: 10.1016/S0080-8784(01)80152-6.

(11) Toriyama, M. Y.; Carranco, A. N.; Snyder, G. J.; Gorai, P. Material Descriptors for Thermoelectric Performance of Narrow-Gap Semiconductors and Semimetals. *Mater. Horiz.* **2023**, *10* (10), 4256–4269.

(12) Stathokostopoulos, D.; Chaliampalias, D.; Stefanaki, E. C.; Polymeris, G.; Pavlidou, E.; Chrissafis, K.; Hatzikraniotis, E.; Paraskevopoulos, K. M.; Vourlias, G. Structure, Morphology and Electrical Properties of Mg_2Si Layers Deposited by Pack Cementation. *Appl. Surf. Sci.* **2013**, *285*, 417–424.

(13) Gaultois, M. W.; Sparks, T. D.; Borg, C. K. H.; Seshadri, R.; Bonificio, W. D.; Clarke, D. R. Data-Driven Review of Thermoelectric Materials: Performance and Resource Considerations. *Chem. Mater.* **2013**, *25* (15), 2911–2920.

(14) Imai, M.; Ibuka, S.; Isoda, Y. Phase Relationship of Mg_2Si at High Pressures and High Temperatures and Thermoelectric Properties of Mg_9Si_5. *Inorg. Chem.* **2021**, *60* (15), 11394–11400.

(15) Fedorov, M. I.; Zaitsev, V. K.; Isachenko, G. N. High Effective Thermoelectrics Based on the Mg_2Si-Mg_2Sn Solid Solution. *Solid State Phenom.* **2011**, *170*, 286–292.

(16) Imai, Y.; Watanabe, A.; Mukaida, M. Electronic Structures of Semiconducting Alkaline-Earth Metal Silicides. *J. Alloys Compd.* **2003**, *358* (1–2), 257–263.

(17) Whalen, J. B.; Zaikina, J. V.; Achey, R.; Stillwell, R.; Zhou, H.; Wiebe, C. R.; Latturner, S. E. Metal to Semimetal Transition in CaMgSi Crystals Grown from Mg–Al Flux. *Chem. Mater.* **2010**, *22* (5), 1846–1853.

(18) Vasquez, G.; Latturner, S. E. Metal Flux Growth of Complex Alkaline Earth/Rare Earth Metal Silicides with a Homologous Series of Metal Phosphide Structure Types. *Chem. Mater.* **2018**, *30* (18), 6478–6485.

(19) Silsby, K.; Sui, F.; Ma, X.; Kauzlarich, S. M.; Latturner, S. E. Thermoelectric Properties of $Ba_{1.9}Ca_{2.4}Mg_{9.7}Si_7$: A New Silicide Zintl Phase with the $Zr_2Fe_{12}P_7$ Structure Type. *Chem. Mater.* **2015**, *27* (19), 6708–6716.

(20) Sheldrick, G. *SAINT (Version 6.02), SADABS (Version 2.03)*. Bruker AXS Inc: Madison, WI, 2002.

(21) Sheldrick, G.; S, N. *Version 6.1, Bruker AXS*. Bruker AXS Inc: Madison, WI, 2000.

(22) Blöchl, P. E.; Jepsen, O.; Andersen, O. K. Improved Tetrahedron Method for Brillouin-Zone Integrations. *Phys. Rev. B* **1994**, *49* (23), 16223–16233.

(23) Tank, R.; Jepsen, O.; Burkhardt, A.; Andersen, O. K. The TB-LMTO-ASA Program. *Max-Planck-Inst. F̈ur Festkörperforschung Heisenbergstr 1D-70569 Stuttg. Fed. Repub. Ger.* **2000**.

(24) Vasquez, G.; Wei, K.; Choi, E. S.; Baumbach, R.; Latturner, S. E. Magnesium-Based Flux Growth and Structural Relationships of a Large Family of Tetrelide Semimetals. *Cryst. Growth Des.* **2020**, *20* (4), 2632–2643.

(25) Meisner, G. P.; Morelli, D. T.; Hu, S.; Yang, J.; Uher, C. Structure and Lattice Thermal Conductivity of Fractionally Filled Skutterudites: Solid Solutions of Fully Filled and Unfilled End Members. *Phys. Rev. Lett.* **1998**, *80* (16), 3551–3554.

(26) Imai, M.; Sato, A.; Matsushita, Y. Effect of Temperature on the Crystal Structure of BaSi2. *Phys. B Condens. Matter* **2019**, *572*, 302–307.

(27) Widera, A.; Schäfer, H. Preparation and Crystal Structure of Ba2Si. *Z. Für Naturforschung B* **1976**, *31* (10), 1434–1435.

(28) Yamanaka, S.; Enishi, E.; Fukuoka, H.; Yasukawa, M. High-Pressure Synthesis of a New Silicon Clathrate Superconductor, Ba8Si46. *Inorg. Chem.* **2000**, *39* (1), 56–58.

(29) Fässler, T. F. Relationships Between Soluble Zintl Anions, Ligand-Stabilized Cage Compounds, and Intermetalloid Clusters of Tetrel (Si–Pb) and Pentel (P–Bi) Elements. In *Zintl Ions: Principles and Recent Developments*; Fässler, T. F., Ed.; Springer Berlin Heidelberg: Berlin, Heidelberg, 2011; pp 91–131. DOI: 10.1007/430_2010_33.

(30) Widera, A.; Eisenmann, B.; Schäfer, H. Notizen: Darstellung Und Kristallstruktur Des Sr2Si/Preparation and Crystal Structure of Sr_2Si. *Z. Für Naturforschung B* **1976**, *31* (4), 520–521.

(31) Evers, J.; Oehlinger, G.; Weiss, A. Notizen: Einkristall-Daten Der Hochdruck- Hochtemperaturphase von $SrSi_2$/Single Crystal Data

of the High Pressure-High Temperature Phase of $SrSi_2$. *Z. Für Naturforschung B* **1983**, *38* (7), 899−900.

(32) Kauzlarich, S. M.; Zevalkink, A.; Toberer, E.; Snyder, G. J. Zintl Phases: Recent Developments in Thermoelectrics and Future Outlook. In *Thermoelectric Materials and Devices*; Nandhakumar, I., White, N. M., Beeby, S., Eds.; The Royal Society of Chemistry, 2016; p 0. DOI: 10.1039/9781782624042-00001.

(33) Kauzlarich, S. M. Special Issue: Advances in Zintl Phases. *Materials* **2019**, *12* (16). 2554.

(34) Franz, R.; Wiedemann, G. Ueber Die Wärme-Leitungsfähigkeit Der Metalle. *Ann. Phys.* **1853**, *165* (8), 497−531.

(35) Chen, J.; Meng, L. Effects of Different Phonon Scattering Factors on the Heat Transport Properties of Graphene Ribbons. *ACS Omega* **2022**, *7* (23), 20186−20194.

(36) Tritt, T. M. *Thermal Conductivity: Theory, Properties, and Applications*; 2010.

(37) Christensen, S.; Schmokel, M. S.; Borup, K. A.; Madsen, G. K. H.; McIntyre, G. J.; Capelli, S. C.; Christensen, M.; Iversen, B. B. ″Glass-like″ Thermal Conductivity Gradually Induced in Thermoelectric $Sr_8Ga_{16}Ge_{30}$ Clathrate by Off-Centered Guest Atoms. *J. Appl. Phys.* **2016**, *119*, No. 185102.